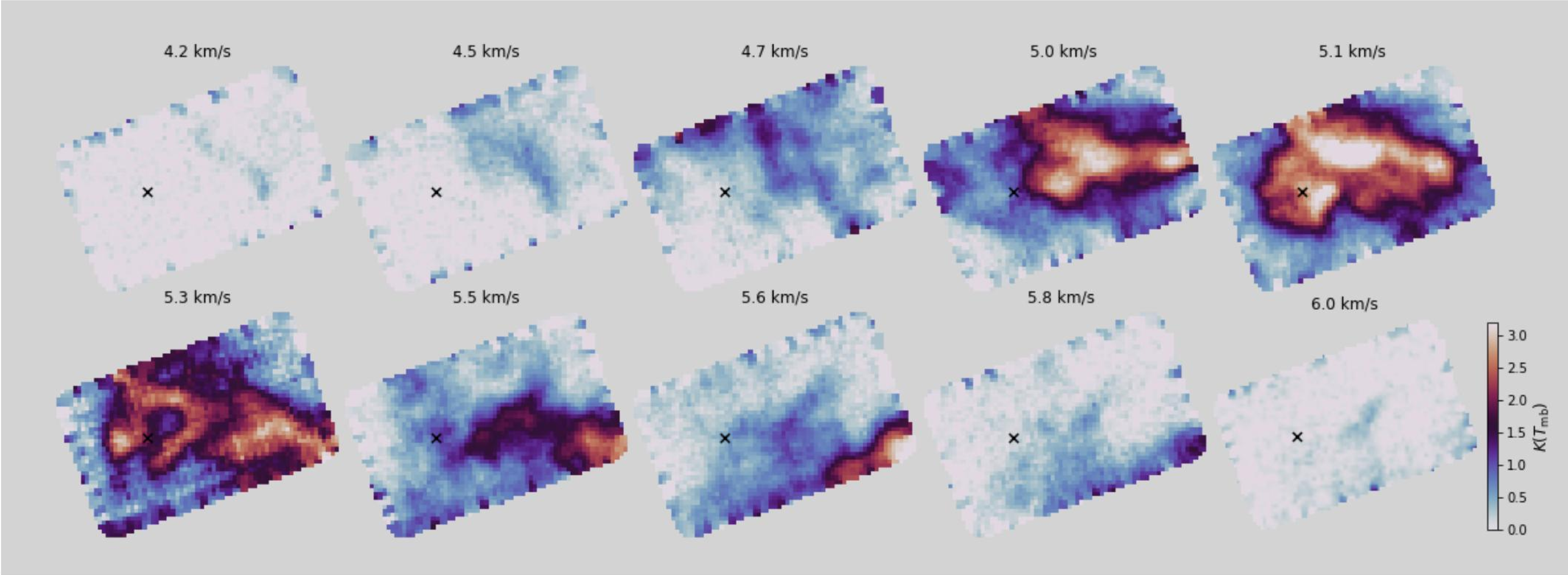

Fig. 2: Channel maps of $C^{18}O$ (2-1) emission. The black cross indicates the position of the protostar core. The velocity of each channel is shown above each panel.

(2-1) spectrum. The blue curves represent the fit when the code uses a two-Gaussian and the green curves are the fit when the code used one Gaussian for the $C^{18}O$ (2-1) line. The vertical line is V_{sys} = 5.2 km s^{-1}, which is the systematic velocity computed from $C^{18}O$ (2-1) line which was reported in Yen et al. (2017) ($V_{sys} = 5.24 \pm 0.03$ km s^{-1}), which is consistent with the systematic velocity seen in our data.

The DCO^+ (3-2) spectra always show a single velocity component with a Gaussian profile. This line traces only one velocity component that is associated with the high-density material. On the other hand, as already mentioned, $C^{18}O$ (2-1) shows two velocity components in their profiles. The brightest component is the one close to the velocity of the DCO^+ (3-2) line, and it hence arises from the high-density material. The fainter component of $C^{18}O$ (2-1) can appear on the red or blue side of the stronger component depending on the location in the cloud. In total, there are three different velocity components, the main one at 5.2 km/s (in all panels on all DCO^+ (3-2) spectra locations), a lower velocity component seen in the northwestern panels, and a higher velocity component seen in the southwestern panels. In the first two rows of Fig. 3 the faint component appears on the blue side, and in the two bottom rows of the spectrum grid it appears on the blue side of the stronger component.

In Fig. 3 we can see the line profiles change across the grid. The multiple velocity components of $C^{18}O$ (2-1) along the line of sight appear to merge from east to west (moving toward the position of the protostar). $C^{18}O$ (2-1) is a lower density tracer than DCO^+ (3-2); these fainter velocity components, seen only in the former tracer, are likely additional nearby low-density filamentary clouds along the line of sight. The core envelope then appears to be found in the correspondence of the merger of these structures. In the following subsections, we discuss the maps of the kinematics parameters for each tracer individually.

4.3. DCO^+ (3-2) line

In Fig. 4 (top panel) we show the velocity dispersion map, which presents a clear increase toward the center of the protostar envelope, starting with very narrow lines in the outer region (around the filament). The mean velocity dispersion derived from DCO^+ (3-2) of the gas in the filament is in fact $\langle\sigma_V\rangle$ = 0.12 ± 0.02 km s^{-1}, but it becomes broader toward the center; for the positions where N(H_2) > 3.2×10^{22} cm^{-2} (inner contour in the Fig. 4), we derive $\langle\sigma_V\rangle$ = 0.175 ± 0.006 km s^{-1}. This increase is linked to the protostellar activity, injecting turbulence, and it could also be caused by the rotation of the core.

We also observe oscillatory motions in the velocity field (visible in the $C^{18}O$ data as well, see Fig. 7, the green dots), which have been seen before in the large-scale velocity patterns. This velocity pattern is consistent with core-forming motions (Hacar & Tafalla 2011). A small velocity gradient can be seen along the filament, which could be linked to the ongoing accretion material toward the central object.

The filament extends over ∼ 0.1 km s^{-1} in velocity toward the protostar from 5.1 km s^{-1} in the west side to 5.0 km s^{-1} at the eastern edge. These positions are shown with red plus signs in Fig. 4. We determine a conservative estimate of the length of the filament of 0.11 pc. This value is computed based on the H_2 column density from *Herschel* data, an area with a higher value than 1.5 × 10^{22} cm^{-2}. In this border we find almost all of the filament (second contour in Fig. 4). Thereby the velocity gradient is $\nabla V = \Delta V/\Delta R = 0.91 \pm 0.23$ kms^{-1}pc^{-1}. To compute the mass of filament we employ this relation:

$$M_{\rm fil} = \sum_{i=1} N(\mathrm{H_2})_{\rm i} \times \mu \times \mathrm{m_H} \times \mathrm{A}. \qquad (3)$$

In this case, we obtain $M_{\rm fil} = 1.04 M_\odot$, where N($H_2$) is gas column density of the $i_{\rm th}$ pixel and A is the area of the pixel; $\mu = 2.8$ and m_H are gas mean molecular weight per hydrogen molecule and hydrogen mass, respectively. Therefore, we quantify the mass accretion rate along the filament, $\dot{M}_{\rm acc} = M_{\rm fil} \times \nabla V = 9.7 \times 10^{-7} M_\odot \mathrm{yr}^{-1}$. This value is affected by some sources of uncertainty. We consider a 2% error on the distance (Dzib et al. 2018), a 12% error on the calibration, and a 40% error due to the assumption of the dust opacity index (Benedettini et al. 2018; Roy et al. 2014). The uncertainty on the mass estimation with all these three errors is a total of 42%. With the 26% error on the velocity gradient, we get a final relative error of 49% for the value of the mass accretion rate. In addition, the inclination of the filament with respect to the plane of the sky is unknown, and it has an influence on the value of $\dot{M}_{\rm acc}$ by a factor of tan i (see, e.g., Chen et al. 2019). The derived value of the accretion